

Quantitative Detection of Single Molecules in Fluorescence Microscopy Images

Eric M. Peterson and Joel M. Harris*

*Department of Chemistry, University of Utah, 315 South 1400 East
Salt Lake City, Utah 84112-0850 USA*

ABSTRACT

Fluorescence imaging and counting of single molecules adsorbed or bound to surfaces is being employed in a number of quantitative analysis applications. Reliable molecular counts with knowledge of counting uncertainties, both false-positive and false-negative probabilities, are critical to these applications. By counting stationary single molecules on a surface, spatial criteria may be applied to the image analysis to improve confidence in detection, which is especially critical when detecting single fluorescent labels. In this work, we describe a simple approach to incorporating spatial criteria for counting single molecules by using an intensity threshold to locate regions with multiple, adjacent intense pixels, where the size of these regions is guided by the point-spread function of the microscope. By requiring multiple, spatially-correlated bright pixels, false-positive events resulting from random samples of background noise are minimized. The reliability of detection is established by quantitative knowledge of the distributions of background and signals. By measuring and modeling both the background and single-molecule intensity distributions, false-positive and false-negative detection probabilities are estimated for arbitrary threshold parameters by using combinatorial statistics. From this theory, detection parameters can be optimized to minimize false-positive and false-negative probabilities, which can be calculated explicitly. For detection of single rhodamine-6G molecules at a threshold set at 2.5-times the standard deviation above background, the false-negative probability was only 1.5%, determined from distributions of single-molecule intensities on well populated surfaces, and the false-positive probability from background noise was 2.8 spots per $50 \times 50\text{-}\mu\text{m}$ image. The false-positive events compare favorably with theoretical probabilities calculated using combinatorial statistical analysis, and simulated false-positive events counted in images of random noise.

*Corresponding author: E-mail: harrisj@chem.utah.edu

INTRODUCTION

Single-molecule fluorescence imaging microscopy has become an important technique for probing a variety of chemical phenomena, including imaging molecular diffusion at interfaces and in nanoporous materials,¹⁻⁶ biomolecular binding interactions,⁷⁻¹⁰ kinetic studies of single enzymes,¹¹⁻¹⁴ and imaging of biomolecules with sub-diffraction resolution to investigate the structure of cells.¹⁵⁻²¹ Single-molecule fluorescence imaging is also being developed as a quantitative analysis tool, where counting fluorescent spots in an image is related to a surface population of bound molecules. This approach has been applied to an *ex situ* analysis where fluorescent molecules are deposited onto a surface by controlled withdrawal of a substrate from solution, followed by imaging of the surface after evaporation of the solvent.²² This method allows quantitative sampling of molecules onto surfaces from low concentration (pM) solutions. Imaging and counting of single molecules on surfaces can also be used to measure adsorption equilibria and kinetics;^{9, 23, 24} when these measurements are made *in situ*,^{9, 23} they require exclusion of signal from the solution-phase and are performed with total-internal-reflection excitation of the solid-liquid interface. Single-molecule imaging has also been employed to count the density of molecules covalently bound to a surface.^{25, 26} Fluorescence imaging can also quantify binding from solution of labeled analyte molecules to reaction sites immobilized on a surface, where the fraction of sites with bound molecules can be related to their concentrations in solution.^{8, 10, 27, 28} In experiments that measure chemical quantities using fluorescence images, it is critical to understand the systematic uncertainties in the methods used to count single molecules in images. For this reason, there is a need for single molecule imaging methodology that optimizes image analysis for detecting molecular events while excluding the influence of background noise and allowing for explicit determination of experimental uncertainties arising from false-positive and false-negative detection probabilities.

Counting single molecules adsorbed or bound to a surface is generally more reliable than counting them in free or flowing solution²⁹⁻³¹ because molecules remain stationary in the image, which allows signal to be integrated over time to the limit of either photobleaching or the residence time of the molecule on the surface or binding site. A second potential advantage of counting stationary single molecules on a surface is that the imaged fluorescent spot may be subjected to spatial criteria that improve confidence in detection; this is critical when counting single fluorescent labels, where the observed intensities are generally close to background noise levels.

In this paper, we describe a simple approach to incorporating spatial criteria for counting single fluorescent dye molecules by using a local intensity threshold to locate regions with multiple, adjacent intense pixels, where the size of the regions is guided by the point-spread function of the microscope. By requiring multiple, spatially correlated bright pixels, false-positive events resulting from random samples of background noise are minimized, which allows molecules can be reliably detected and counted at a threshold that is nearer the background noise level. Setting thresholds closer to the background noise level is required for reliable detection of single-fluorescent labels, where spatial criteria for detection can lower false-positive probabilities by factors of 600 or more, to acceptable levels for quantitative work. The reliability of detection is established by quantitative knowledge of the distributions of background and signals.³² By measuring and modeling both the background and single-molecule intensity distributions, false-positive and false-negative detection probabilities can be estimated for arbitrary threshold parameters by using simple counting statistics. From this theory, detection parameters can be optimized to minimize false-positive and false-negative probabilities, which can be calculated explicitly.

In order to develop this analysis, controlled surface densities of rhodamine 6G were deposited onto glass coverslips by substrate withdrawal from varying concentrations of dye in methanol solution, as his method has been shown to generate predictable and quantitative surface fluorophore coverage predicted from the solvent viscosity, density, contact angle and withdrawal rate.^{22, 33-35} The fluorescence from single molecules was imaged by through-the-objective total-internal-reflection-fluorescence (TIRF)³⁶ microscopy. Histograms of the photoelectron counts from background regions and from regions of fluorescent spots of single molecules were acquired from images and used to establish the detection threshold and quantify false-negative probabilities, β . False-positive probabilities, α , are quantified by applying the single-molecule detection algorithm to blank images, and compared to modeling of simulated images using a combinatorial statistical analysis.

EXPERIMENTAL SECTION

Chemicals and Materials. Spectroscopic grade methanol was purchased from Fisher Scientific (Hampton, NH) and used as received. Concentrated 95% sulfuric acid (EMD Chemicals) and 30% hydrogen peroxide solution ACS grade (EMD Chemicals) were purchased from VWR (West Chester, PA) and used as provided. Water was distilled in a quartz still and then further filtered with a Barnstead NANOpure® II system (Boston, MA) resulting in a resistivity of approximately 18 M Ω -cm. Rhodamine 6G (R6G) 99% purity (Acros Organics) was purchased from Fisher Scientific (Hampton, NH) and used as received. Glass 22 x 22 mm no. 1 coverslips were purchased from VWR (West Chester, PA).

Deposition of dye molecules onto glass. Glass coverslips were prepared with known densities of rhodamine 6G molecules by withdrawing them from standard solution at a controlled velocity.^{22, 35} Prior to dye deposition, glass coverslips were cleaned by rinsing in 18 M Ω water for 15 minutes, followed by 15 minutes of exposure to piranha solution (3:2 mixture of

concentrated sulfuric acid and 30% hydrogen peroxide). After piranha cleaning, the coverslips were rinsed in 18 M Ω water and methanol twice each for 10 minutes, allowed to dry, and then cleaned in a UV ozone cleaner (Jelight Co. model 342) for 25 minutes per side. A blank methanol sample plus R6G solutions in methanol were prepared at concentrations of 20, 40, 79, 155, and 283 pM for deposition. During deposition, the glass coverslip is held stationary in clamp above a moving platform that supports a beaker containing the blank or R6G solution. The platform is attached to a Velmex UniSlide platform mounted vertically on an angle bracket and driven by a Pittman stepper motor. The platform is first raised until the solution covers the coverslip substrate, and then the platform is immediately lowered until the surface of the solution drops below the bottom edge of the substrate, leaving a thin solution film on its surface. The thin film deposited on the slide is allowed to evaporate, and one side of the coverslip is wiped with methanol-wetted lens tissue to remove any deposited dye from the surface that will be in contact with immersion oil of the microscope objective.

Fluorescence Microscopy. R6G coated glass coverslips were imaged using an Olympus iX71 inverted microscope with through-the-objective total-internal-reflection-fluorescence (TIRF) illumination. Laser radiation at 514 nm from a Coherent® Innova® 300 argon ion laser is coupled into a single mode polarization maintaining optical fiber (Thorlabs) using a fiber collimating lens (Thorlabs). Light emitted from the opposite end of the fiber is collimated by a planoconvex achromatic lens, and passed through a quarter wave plate (Newport). The 1.2 mW collimated laser beam is then focused onto the back focal plane of a 60x 1.45 N.A. oil immersion objective lens. Total-internal reflection is achieved by translating the fiber position horizontally until the laser beam is focused near the edge of the objective's back aperture. Fluorescence emission from the coverslip-air interface is collected by the same objective, passed through a

filter cube with a dichroic beam splitter (Chroma Z514RDC), an emission band pass filter (Chroma HQ560/50m), and then through additional 1.6x magnification optics.

It has been shown previously that linearly polarized illumination can lead to significant variations in single-molecule emission intensity^{7, 37} because random excitation dipole orientations experience varying excitation electric field strengths. For this reason, a quarter-wave plate was used to generate elliptically polarized excitation light with an s-polarized to p-polarized light ratio of 2.5:1, in order to provide a more isotropic light intensity at the interface. This polarization ratio generates approximately equal light intensities both normal to the interface and in the plane of the interface, normal to the reflection axis, in the evanescent wave.³⁸ The laser excitation intensity was minimized in order to prevent photobleaching of the dye molecules. The total laser intensity coupled into the objective lens was 1.2 mW, corresponding to a power density of approximately 16 Wcm^{-2} .

Images were collected with an electron multiplying charge coupled device (EMCCD) camera (Andor™ iXon^{EM+} 897) using a 300 x 300 pixel region on the sensor ($50 \times 50 \mu\text{m}$ in the sample). Images were taken by collecting continuous videos at approximately 4 frames per second (275 ms integration time at an EM gain of 54) while translating the microscope stage in x-y manually from region to region on the coverslip. Images from unique regions were then cut out of the video and analyzed.

Data Analysis. Image processing and analysis were carried out using custom programs written in the Matlab® (Mathworks™) software environment. Analysis was largely performed on a PC with an Intel® 3 GHz Core™ 2 Duo processor and 8 GB of RAM running a 64 bit operating system. Single R6G molecules were located in each image using an automated routine which records the location and pixel intensity of each spot for analysis. The details of the algorithm are described below.

RESULTS AND DISCUSSION

Quantitative imaging of rhodamine 6G on glass. R6G molecules deposited on glass slides by substrate-withdrawal from standard solutions^{22, 35} were imaged using an inverted microscope with through-the-objective TIRF illumination at 514 nm from an argon ion laser. An example image is shown in Figure 1. Low laser excitation intensity, approximately 16 Wcm^{-2} , was used in order to minimize photobleaching of the fluorophore. The photobleaching rate was determined by observing R6G molecules bleach on the glass surface upon continuous exposure to laser radiation. A plot of the number of surviving molecules on the surface versus time has been fit to a biexponential decay function in order to determine the photobleaching rates; see Supporting Information. The photobleaching rates are 0.22 s^{-1} and 0.014 s^{-1} , with relative pre-exponential factors of 0.71 and 0.29, respectively. To reduce the intensity variation due to photobleaching, the fraction of R6G lost to photobleaching was kept below 10% by collecting images within 0.8 seconds of illuminating a new region.

Images of single molecules were collected using an Andor iXon EMCCD camera using a low electron multiplying gain setting of 54, out of a maximum of 1000. The pixel intensity values in all images were converted from analog-to-digital unit (ADU) counts to actual photoelectron counts using calibration images of flat white-light background noise.³⁹ The ADU count variance in white light images measured with varying integration times was plotted against the corresponding ADU count mean, and fit to a linear function. The white light intensity-variance curve fit a straight line (see Supporting Information), indicating Poisson behavior in the measured background intensities. The x-intercept of this fitted line is used correct for the detector offset, and the slope is used to convert between ADU counts and photoelectrons.³⁹

Single-molecule spots in images were located using a detection algorithm that takes into account the size of the point-spread function of the microscope, which causes the images of

single-molecule fluorescence spots to be distributed over several adjacent pixels on the CCD camera. This information can be used to exclude random noise from the detector by requiring that the intensity of detected molecular spots be spatially correlated, where several adjacent pixels are above a threshold. The choice of the number of adjacent bright pixels in the detection algorithm is based on the measured intensity distribution of single R6G molecules. This point-spread function (PSF) was determined by fitting a two-dimensional symmetrical Gaussian function to each of approximately 1,500 bright spots in an image; see example in Figure 2. From the average parameters extracted from these fits, the point-spread function was well modeled by a Gaussian spatial distribution with a radius (standard deviation) of 1.0 ± 0.2 pixels (16 μm on the camera, 170 nm in the sample). The radius of this distribution predicts that at 1 pixel away from center, the intensity will be 60% of the maximum signal at the center; while at 2 pixels away from the center, the intensity will be down to 13%. Pixels with only 13% of the brightness of the peak pixels are likely to be indistinguishable from noise, and so only pixels adjacent to the center of the PSF, estimated as the brightest pixel in the measured PSF, will be detectable. There are 8 pixels adjacent to any maximum pixel, resulting in a detection volume of 3×3 pixels or 9 pixel^2 (500 \times 500 nm in the sample). The distribution of individual pixel intensities in this detection volume can vary significantly due to variations in the position of the point-spread function in relation to the pixel locations. The smallest number of illuminated pixels is observed when the single-molecule intensity distribution is centered on the corner of four adjacent pixels, where those four pixels would accumulate most of the intensity. Moving the center of the distribution off of this corner increases the number of illuminated pixels that receive up to 60% of the maximum (see above). To assure that molecules are detected even when their intensity falls on a corner, we conservatively set the detection criterion such that two adjacent pixels, $p_{\text{crit}} = 2$, next to any bright pixel must also be above threshold. Note that adjacent bright pixels can share a

corners or edges, and the criterion could be set higher than 2 if the point-spread function were larger relative to the pixel dimensions.

The algorithm for identifying spatially correlated bright pixels first requires a threshold for detecting significant signal intensity above background. This intensity threshold, I_{thold} , is defined as some multiple, n_{thold} , of the standard deviation of the background, σ_{BG} , above the mean background, μ_{BG} :

$$I_{\text{thold}} = \mu_{\text{BG}} + n_{\text{thold}} \sigma_{\text{BG}} \quad (1)$$

For each set of images, μ_{BG} and σ_{BG} were determined by fitting a Gaussian distribution to a histogram of photoelectron counts. The distribution of photoelectron counts in blank images follows a Poisson shot noise model, where the mean background value, 13.6 counts, is equivalent to the background variance, 13.3 counts. In order to accurately determine the Poisson mean, μ_{BG} , the histogram of blank intensities was fit to a Poisson distribution using least-squares methods. The blank intensity histogram and fitted Poisson distribution, with $\mu_{\text{BG}} = 13.0$ photoelectrons as the only fitted parameter, is plotted in Figure 3.

When R6G molecules are present in an image, the upper tail of the background intensity distribution is perturbed by the presence of bright single-molecule spots, making it impossible to fit a Poisson distribution. In order to circumvent this problem, the mean background in R6G images is estimated from a Gaussian fit and the standard deviation is estimated as: $\sigma_{\text{BG}} = \mu_{\text{BG}}^{1/2}$. A fit of the background intensity to a symmetrical Gaussian distribution slightly overestimates the Poisson mean because it does not capture the Poisson tail at high intensities; nevertheless, the error is less than 5% for a mean of 13 photoelectrons, and the error becomes smaller as the mean increases.^{40, 41} The 20, 40 and 79 pM R6G samples were found to have very similar μ_{BG} and σ_{BG} values, and so a single I_{thold} was chosen to simplify the false-positive probability calculation (see below). The background distribution parameters, μ_{BG} , σ_{BG} , and I_{thold} , are summarized in Table 1.

Having established an intensity threshold, I_{thold} , for identifying adjacent bright pixels for detection of single molecules, the algorithm finds the brightest pixel in an image and then tests the eight adjacent pixels around that bright pixel to determine the number, q , that exceed I_{thold} . When $q \geq p_{\text{crit}} = 2$, then the bright spot is counted as a single molecule. Before locating the next highest bright spot in the image, the previous spot must be prevented from being double counted; therefore, a small region, typically 7×7 pixels ($1.17 \times 1.17 \mu\text{m}$), around the spot is deleted from the search for brightest pixels. The algorithm then steps to the next brightest pixel in the image and the process repeats. An example image of R6G molecules deposited on glass out of a 79 pM R6G methanol solution is shown in Figure 1, along with the identified spots from the search algorithm. Measured R6G surface densities deposited on substrates from solutions with varying R6G concentration are shown in Figure 4.

Verifying the detected molecular density with standards. In order to verify the accuracy of the measured surface densities reported by the single-molecule detection algorithm, standard samples having known, optically-resolvable fluorophore densities are required. Samples that meet these criteria were generated by dosing glass substrates with rhodamine 6G by substrate-withdrawal from standard solutions.^{22, 34, 35} This technique is based on theory by Landau and Levich,⁴² which predicts the thickness of a liquid layer, t , that adheres to a solid surface above the liquid meniscus, as the substrate is withdrawn from the liquid at a velocity, U :

$$t = \frac{0.994(\eta U)^{2/3}}{(\rho g)^{1/2} \gamma^{1/6}} \quad (2)$$

This thickness was evaluated for methanol as a solvent, where the density, $\rho = 791.4 \text{ kg/m}^3$, the viscosity, $\eta = 5.97 \times 10^{-4} \text{ kg/m}\cdot\text{s}$, the surface tension, $\gamma = 2.61 \times 10^{-3} \text{ N/m}$, and gravitational acceleration, $g = 9.81 \text{ m/s}^2$. At a withdrawal rate, $U = 0.60 \text{ cm/s}$, the predicted film thickness is $t = 5.0 \mu\text{m}$. If the solution contains a known concentration of fluorophores, C , the resulting

density of molecules, Γ , that remain on the surface after solvent evaporation is the solution concentration times the film thickness,^{22, 35}

$$\Gamma = C t \quad (3)$$

If the fluorophore being deposited has strong interactions with the solid surface, the observed surface density could be higher than that predicted due to adsorption from solution prior to withdrawal. Adsorption of rhodamine 6G to silica surfaces has been tested by measuring its elution by methanol from a silica gel column using HPLC.^{22, 35} The adsorption equilibrium constant of rhodamine 6G was determined from the measured capacity factor, k' , mobile-phase volume and mass of silica gel in the column, and the specific surface area of the silica gel. The adsorption equilibrium constant of the dye onto silica from methanol was found to be small, $K_{ads} = \Gamma_{ads} / C = 2.5 \times 10^{-6} \text{ cm} = 0.025 \text{ }\mu\text{m}$.²² This equilibrium constant is the ratio of the density of dye on the surface to the concentration of dye in solution and is the equivalent solution depth that contains the same number of molecules per unit area as are adsorbed to the surface at equilibrium. This solution depth can be compared directly to the adherent solution film following withdrawal from solution, to determine whether adsorption or deposition governs the number of molecules per unit area on the surface.²² Compared to the thickness of the liquid film that adheres to the substrate upon withdrawal from solution, $t = 5.0 \text{ }\mu\text{m}$, the adsorption equilibrium constant corresponds to an equivalent solution depth that is a small fraction (0.5%) of the deposited solution film thickness (at the withdrawal velocity, $U = 0.60 \text{ cm/s}$). Therefore, adsorption of R6G prior to substrate withdrawal from solution will account for an insignificant number of molecules on the surface compared to those deposited by evaporation of the adherent solution film. From the R6G concentrations used in depositing dye for this work, 20 to 280 pM, the predicted surface densities range from $\Gamma = 6.0 \times 10^6$ to $8.5 \times 10^7 \text{ cm}^{-2}$, and are plotted in Figure 4.

As Figure 4 shows, the predicted R6G surface deposition density, Γ , agrees with measured results at low concentrations, but is higher than the measured surface density at higher concentrations. The lower measured densities are due to the algorithm being unable to resolve multiple molecules within the 7×7 pixel area corresponding to a detected spot and deleted from further searching. This area represents the resolution limit for locating and counting single molecules. At higher surface densities, the distances between molecules approach this resolution limit, and the number of spots counted will be less than the actual number of deposited molecules, as individual single-molecule spots fail to be resolved. Because the countable numbers of molecules on the surface are drawn with low probability from a much larger population in solution and dispersed randomly over the surface, the occupation of resolvable areas on the surface and the likelihood of multiple occupation molecular overlap should follow Poisson statistics.⁴⁰

Poisson statistics have been used to account for peak overlap developed for chromatographic separations,⁴³ saturation of single-molecule counting in capillary electrophoresis,²⁹ and more recently to estimate the peak capacity single-molecule images.²² This Poisson model predicts the measured density of spots in an image from the maximum density of resolvable spots, D_{\max} , times one minus the probability of no molecules being detected:

$$D_{\text{meas}} = D_{\max} [1 - \exp(-\Gamma/D_{\max})] \quad (4)$$

where D_{meas} is the measured spot density, Γ is the actual molecular coverage, and D_{\max} is the density of spots that can be resolved. D_{\max} can be calculated explicitly for the detection algorithm above using the size of the region that is deleted from the search for brightest pixels after every detected spot is found. A 7×7 pixel region is deleted around each detected spot, meaning that the closest bright spot can be 4 pixels away. Starting in the corner of the image and arranging spots 4 pixels apart in x and y, a 300×300 pixel image can be occupied by $300^2 / 4^2 =$

5625 spots, corresponding to $D_{\max} = 2.25 \times 10^8$ spots/cm². Using this value of D_{\max} , the measured density of spots D_{meas} can be predicted from Equation 4 with the molecular density predicted by Equation 3. In Figure 4, the *a priori* predictions of Equation 4, *which are not fitted to the measured surface densities*, are plotted together with the measured results, which agree within the uncertainty of the measurements.

Determining false-negative probability. The false-negative detection probability, β ,³² is the fraction of single-molecule spots that do not exceed the intensity threshold, I_{thold} . Because the algorithm used to identify single-molecule spots requires that three adjacent pixels be brighter than I_{thold} , successful detection depends entirely on the intensity of the third-most-intense pixel within the point-spread function. For convenience, this critical, third-most-intense pixel will be called "pixel-3." We can determine β by fitting a histogram of pixel-3 intensities from each located single-molecule spot to a distribution in order to determine what fraction of the pixel-3 distribution lies below I_{thold} .

A histogram of pixel-3 intensities from images of samples deposited from 155-pM R6G solution is shown in Figure 5; these data are fit to an empirical, asymmetric double-sigmoid function,⁴⁴ which follows the observed histogram shape over its entire range. The asymmetry of the single-molecule intensity distribution is due in part to the random orientation of molecules on the surface which affects the excitation and collection efficiency;⁴⁵ additional intensity variation arises from the sampling of the point-spread function by the 3rd pixel, which depends sensitively on position of the spot relative to the pixel array. The fitted distribution in Figure 5 is integrated numerically to determine the total area and the area that is below the threshold, I_{thold} . The ratio of the area below threshold to the total area defines β , which was found to be 1.2%. The 155 pM and 283 pM images contained sufficient molecule spots (greater than 70,000) to generate clean histograms and β statistics. For the 20, 40 and 79 pM images it was necessary to sum their

pixel-3 histograms to collect sufficient observations to determine β . Because the mean backgrounds and standard deviations were very close for these lower-density samples, the same I_{thold} was used for the 20, 40, and 79 pM images which also allowed the histogram areas from these data to be combined. The average β for all data sets (see Table 1) was found to be 2.5%, indicating that 97.5 % of all R6G molecules are detected, which is consistent with the measured molecular densities agreeing with the substrate-withdrawal standards, described in the previous section. The slightly higher false-positive probability in the lower concentration samples, 4.4%, is an artifact of false-positive events, which comprise a greater fraction of the detected spots in lower density images. False negative probabilities determined for n_{thold} values between 1.5 and 3.5 have been calculated by numerical integration of the empirical function fit to the 155 pM pixel-3 distribution, and are plotted in Figure 6A.

Determining false-positive probability. A major advantage of this multi-pixel single-molecule detection scheme is that false-positive detection probabilities can be calculated explicitly, using combinatorial statistical analysis,⁴⁶ from the detection algorithm parameters and the background intensity distribution. These mathematical techniques are analogous to calculating statistical thermodynamics partition functions. Theoretical false-positive probabilities, $\alpha_{(\text{theor})}$ are defined by the number ways to arrange intense pixels derived from noise that trigger a false positive, N_{detect} , divided by the total number of ways intense noise pixels can be arranged, N_{total} :

$$N_{\text{total}} = \frac{p_{\text{total}}!}{p_{\text{thold}}!(p_{\text{total}} - p_{\text{thold}})!} \quad (5)$$

N_{total} is calculated from the number of pixels in an image, p_{total} , and the number of noise pixels, p_{thold} , brighter than the intensity threshold, I_{thold} . For background noise comprised of photoelectron shot noise, p_{thold} is calculated by multiplying p_{total} by the integral of the

background Poisson distribution that is above the intensity threshold for detection, I_{thold} . N_{detect} is defined as the number of ways p_{crit} pixels above I_{thold} can be arranged in p_{adj} pixels adjacent to p_{thold} pixels above I_{thold} , multiplied by the number of ways the remaining $p_{\text{thold}} - p_{\text{crit}}$ pixels can be arranged in the entire image. This expression must then be summed over an index q from p_{crit} to p_{adj} . Finally, this value is multiplied by the total number of pixels above threshold, p_{thold} , to generate an expression for N_{detect} :

$$N_{\text{detect}} = \sum_{q=p_{\text{crit}}}^{q=p_{\text{adj}}} \frac{p_{\text{thold}} \cdot p_{\text{adj}}! (p_{\text{total}} - p_{\text{adj}})!}{q! (q - p_{\text{adj}})! (p_{\text{thold}} - q)! (p_{\text{total}} - p_{\text{adj}} - p_{\text{thold}} + q)!} \quad (6)$$

Dividing N_{detect} by N_{total} yields the final expression for the theoretical false-positive probability per video frame, α_{theor} :

$$\alpha_{\text{theor}} = \frac{p_{\text{thold}} \cdot p_{\text{adj}}! p_{\text{thold}}! (p_{\text{total}} - p_{\text{adj}})! (p_{\text{total}} - p_{\text{thold}})!}{p_{\text{total}}!} \cdot \sum_{q=p_{\text{crit}}}^{q=p_{\text{adj}}} \frac{1}{q! (q - p_{\text{adj}})! (p_{\text{thold}} - q)! (p_{\text{total}} - p_{\text{adj}} - p_{\text{thold}} + q)!} \quad (7)$$

The function was evaluated for only $q = p_{\text{crit}} = 2$, as the probability contribution from larger q is quite small in this case, although it could be greater for spot images that are magnified over a greater number of pixels. The resulting truncated α_{theor} was evaluated, using Stirling's approximation carried to four terms, with the experimental detection parameters used in the blank images (μ_{BG} , σ_{BG}). The accuracy of this expression was tested by locating false-positive spots in simulated images of random, Poisson-like noise modeled after blank images with $\mu_{\text{BG}} = 13.0$ photoelectrons. The simulated false-positive probability, α_{sim} , and the theoretical false-positive probability, α_{theor} , were found to agree within the simulation uncertainty, as shown in Figure 6. At a threshold of 2.5 standard deviations above the background, $n_{\text{thold}} = 2.5$, α_{theor} predicted 1.9 events per 300×300 pixel image, while α_{sim} averaged 2.0 ± 1.4 false positives.

The false-positive probabilities in actual experimental images were determined from blank images of slides that were dip coated by withdrawal from pure methanol containing no R6G. Short 6 to 15 frame videos of 6 stationary regions on blank slides were collected and bright spots were located in each video frame. False-positive probabilities resulting from random noise were determined by counting spots located in only one video frame. Any spots found with the same coordinates in multiple frames were likely the result of actual fluorescent defects in the glass or contamination on the surface and were excluded from the false-positive probability determination. The total blank spot count was 9 ± 3 per image, while the false-positive probability resulting from background noise alone (non-spatially correlated detected spots) was found to be $\alpha = 2.8 \pm 1.6$ false positives per image. The experimentally measured $\alpha = 2.8 \pm 1.6$ FP per image, and theoretical $\alpha_{\text{theor}} = 1.9$ FP per image as shown on Figure 6B, agree remarkably well, further indicating that the background intensity is well modeled by a Poisson distribution. Similar calculations and simulations based on a Gaussian background pixel distribution greatly underestimate the false-positive probability, predicting $\alpha = 0.17$ per image.

False positive rates are significantly reduced by detecting three spatially-correlated intense pixels rather than a single, intense pixel. The false positive rate, for a detection scheme using no spatial correlation criteria where only a single intense pixel is detected, was determined by numerically integrating the background pixel Poisson distribution at varying values of n_{thold} , and the results are also plotted in Figure 6B. At $n_{\text{thold}} = 2.5$ used in our experiments, the single-pixel false positive rate agrees with the prediction and is ~ 600 -times greater (over 1,500 events per frame) than when spatial criteria are added to the detection scheme. Detecting true single molecule events in images with low signal-to-noise ratios typical of a single-fluor response would be impossible without adding spatial criteria to the detection scheme. Finally, a comparison of the false-negative and false-positive results in Figure 6 clearly illustrate the trade-

offs that exist in setting a threshold for single-molecule detection. Lowering the threshold can decrease the probability of missing molecules that should be counted; however lowering the threshold also dramatically raises the numbers of false events that are included in the count. The appropriate trade-off depends on the average molecular density in an image, where greater numbers of true fluors in an image will lower the relative error caused by a higher number of false-positive events allowing a lower threshold. The upper bound to an acceptable molecular density depends on the spot-capacity of the image, D_{\max} , limited by the optical resolution of the microscope.

Summary. The goal of this research was to develop and demonstrate methodology capable of quantitatively detecting single dye labels in fluorescence images. Quantitative, optically-resolvable densities of rhodamine 6G fluorophores were deposited onto glass surfaces and imaged using total-internal-reflection-fluorescence microscopy. Using a multiple-pixel intensity threshold detection algorithm, individual rhodamine 6G dye molecules were located and counted in images of the dye deposited onto glass at varying surface densities. Measured R6G spot densities were shown to correspond to expected molecular coverages, validating the detection algorithm. Theory has been developed to evaluate false-negative and false-positive detection probabilities using simple parameters, such as the background and the single molecule pixel photoelectron distribution, which can be evaluated for any single molecule imaging experiment. False-negative probabilities were evaluated from histograms of located single molecules, and average from higher concentration samples to be 1.5%. False-positive detection probabilities, as measured in blank images and evaluated using theoretical and simulation techniques, were greatly reduced by incorporation of spatial criteria in the analysis, from over 1,500 events per frame to approximately 2 to 3 events per image.

Samples in this experiment were imaged using relatively low laser intensities, with resulting low signal to noise levels, in order to minimize photobleaching, which is critical to measuring the kinetics of molecules carrying a single fluorescent label in order to minimize the influence of photobleaching on the observed kinetics. Despite low signal-to-noise ratios, single dye labels can be reliably detected with reasonable uncertainties. Reliable single-molecule detection is relevant to applications where the results will be subjected to quantitative interpretation (counting molecule populations, measuring residence times). The techniques described in the present work can help to design, optimize, and evaluate the uncertainty in quantitative applications of single-molecule imaging measurements.

ACKNOWLEDGMENTS

This research was supported by the U.S. Department of Energy under grant DE-FG03-93ER14333. Additional support from the National Science Foundation for the construction of the TIRF microscope under grant CHE-0654229, is gratefully acknowledged.

Supporting Information Available. This material is available free of charge via the Internet at <http://pubs.acs.org>.

References

- (1) Schmidt, T.; Schütz, G. J.; Baumgartner, W.; Gruber, H. J.; Schindler, H. *Proceedings of the National Academy of Sciences of the United States of America* **1996**, *93*, 2926-2929.
- (2) Ludes, M. D.; Wirth, M. J. *Analytical Chemistry* **2002**, *74*, 386-393.
- (3) McCain, K. S.; Hanley, D. C.; Harris, J. M. *Analytical Chemistry* **2003**, *75*, 4351-4359.
- (4) He, Y.; Li, H.-W.; Yeung, E. S. *Journal of Physical Chemistry B* **2005**, *109*, 8820-8832.
- (5) Higgins, D. A.; Collinson, M. M. *Langmuir* **2005**, *21*, 9023-9031.
- (6) Lu Li, X. T., Guizheng Zou, Zhikun Shi, Xiaoli Zhang, Wenrui Jin *Analytical Chemistry* **2008**, *80*, 3999-4006.
- (7) Tokimoto, T.; Bethea, T. R. C.; Zhou, M.; Ghosh, I.; Wirth, M. J. *Applied Spectroscopy* **2007**, *61*, 130-137.
- (8) Elenko, M. P.; Szostak, J. W.; van Oijen, A. M. *Journal of the American Chemical Society* **2009**.
- (9) Fox, C. B.; Wayment, J. R.; Myers, G. A.; Endicott, S. K.; Harris, J. M. *Analytical Chemistry* **2009**, *81*, 5130-5138.
- (10) Wayment, J. R.; Harris, J. M. *Analytical Chemistry* **2009**, *81*, 336-342.
- (11) Funatsu, T.; Harada, Y.; Tokunaga, M.; Saito, K.; Yanagida, T. *Nature* **1995**, *374*, 555-559.
- (12) Tokunaga, M.; Kitamura, K.; Saito, K.; Iwane, A. H.; Yanagida, T. *Biochemical and Biophysical Research Communications* **1997**, *9*, 47-53.
- (13) Roeffaers, M. B. J.; De Cremer, G.; Uji-i, H.; Muls, B. o.; Sels, B. F.; Jacobs, P. A.; De Schryver, F. C.; De Vos, D. E.; Hofkens, J. *Proceedings of the National Academy of Sciences* **2007**, *104*, 12603-12609.

- (14) Min, W.; English, B. P.; Luo, G.; Cherayil, B. J.; Kou, S. C.; Xie, X. S. *Accounts of Chemical Research* **2005**, *38*, 923-931.
- (15) Carrington, W. A.; Lynch, R. M.; Moore, E. D. W.; Isenberg, G.; Fogarty, K. E.; Fay, F. S. *Science* **1995**, *268*, 1483-1487.
- (16) Thompson, R. E.; Larson, D. R.; Webb, W. W. *Biophysical Journal* **2002**, *82*, 2775-2783.
- (17) Yildiz, A.; Forkey, J. N.; McKinney, S. A.; Ha, T.; Goldman, Y. E.; Selvin, P. R. *Science* **2003**, *300*, 2061-2065.
- (18) Ober, R. J.; Ram, S.; Ward, E. S. *Biophysical Journal* **2004**, *86*, 1185-1200.
- (19) Juette, M. F.; Gould, T. J.; Lessard, M. D.; Mlodzianoski, M. J.; Nagpure, B. S.; Bennett, B. T.; Hess, S. T.; Bewersdorf, J. *Nature Methods* **2008**, *5*, 527-529.
- (20) Betzig, E.; Patterson, G. H.; Sougrat, R.; Lindwasser, O. W.; Olenych, S.; Bonifacino, J. S.; Davidson, M. W.; Lippincott-Schwartz, J.; Hess, H. F. *Science* **2006**, *313*, 1642-1645.
- (21) Rust, M. J.; Bates, M.; Zhuang, X. *Nature Methods* **2006**, *3*, 793-769.
- (22) Hanley, D. C.; Harris, J. M. *Analytical Chemistry* **2001**, *73*, 5030-5037.
- (23) Wang, L.; Xu, G.; Shi, Z.; Jiang, W.; Jin, W. *Analytica Chimica Acta* **2007**, *590*, 104-109.
- (24) Li, L.; Tian, X.; Zou, G.; Shi, Z.; Zhang, X.; Jin, W. *Analytical Chemistry* **2008**, *80*, 3999-4006.
- (25) Tani, T.; Yamaguchi, Y.; Ohuchi, K.; Oda, M. *Journal of Luminescence* **2004**, *107*, 42-50.
- (26) Wayment, J. R.; Harris, J. M. *Analytical Chemistry* **2006**, *78*, 7841-7849.
- (27) Lee, J.-Y.; Li, J.; Yeung, E. S. *Analytical Chemistry* **2007**, *79*, 8083-8089.
- (28) Jiang, D.; Wang, L.; Jiang, W. *Analytica Chimica Acta* **2009**, *634*, 83-88.
- (29) Chen, D.; Dovichi, N. J. *Analytical Chemistry* **1996**, *68*, 690-696.

- (30) Keller, R. A.; Ambrose, W. P.; Goodwin, P. M.; Jett, J. H.; Martin, J. C.; Wu, M. *Applied Spectroscopy* **1996**, *50*, 12A-32A.
- (31) Fister, J. C.; Jacobson, S. C.; Davis, L. M.; Ramsey, J. M. *Analytical Chemistry* **1998**, *70*, 431-437.
- (32) Currie, L. A. *Analytical Chemistry* **1968**, *40*, 586-593.
- (33) Landau, L.; Levich, B. *Acta Physiochim. U.R.S.S.* **1942**, *17*, 42-54.
- (34) Marques, D.; Costanza, V.; Cerro, R. L. *Chemical Engineering Science* **1978**, *33*, 87-93.
- (35) Lacy, W. B.; Olson, L. G.; Harris, J. M. *Analytical Chemistry* **1999**, *71*, 2564-2570.
- (36) Axelrod, D. *Methods in Cell Biology* **1989**, *30*, 245-270.
- (37) Bartco, A. P.; Dickson, R. M. *Journal of Physical Chemistry B* **1999**, *103*, 11237-11241.
- (38) Hansen, W. *Journal of the Optical Society of America* **1968**, *58*, 380-390.
- (39) Mortara, L.; Fowler, A. *Proc. SPIE* **1981**, *290*, 28-33.
- (40) Barlow, R. J. *Statistics: A Guide to the Use of Statistical Methods in the Physical Sciences*; John Wiley: Chichester, 1989.
- (41) Taylor, J. R. *An Introduction to Error Analysis: The Study of Uncertainties in Physical Measurements*, Second Edition ed.; University Science Books: Sausalito, CA, 1997.
- (42) L. Landau, B. L., *17*, 42-54. *Acta Physiochim. U.R.S.S.* **1942**, *17*, 42-54.
- (43) Davis, J. M.; Giddings, J. C. *Analytical Chemistry* **1985**, *57*, 2168-2177.
- (44) Krustok, J.; Collan, H.; Yakushev, M.; Hjelt, K. *Pysica Scripta* **1999**, *T79*, 179-182.
- (45) Plakhotnik, T.; Moerner, W. E.; Palm, V.; Wild, U. P. *Optics Communications* **1995**, *114*, 83-88.
- (46) Bogart, K. P. *Introductory Combinatorics*; Pitman Publishing Inc.: Marshfield, MA, 1983.

FIGURE CAPTIONS

1. Image of R6G dip-coated onto a glass coverslip from 79 pM R6G solution in methanol. Images show before (left) and after (right) detecting all spots that meet the adjacent-pixel criterion. Image size is 50x50 μm .
2. Example single-molecule fluorescence point-spread function sampled by the CCD camera in the reference frame of the sample. A. Raw intensity data; B. Fitted symmetrical 2-D Gaussian function; C. Residuals of the fit.
3. Histogram of integral-normalized blank image in photoelectron counts, fit to a Poisson distribution with $\mu_{\text{BG}} = 13.0$ photoelectrons
4. Measured dip coated R6G density (black squares) are plotted with expected molecular coverage, Γ (dashed line) and the expected detectable spot density, D_{meas} (full line) from Equation 4; error bars represent 2 standard deviations of the mean.
5. Histogram of pixel intensities for all pixels in the image (black circles) and the third most intense pixel in the single molecule spot (black triangles). The red and green regions represent the area of a double asymmetric sigmoid function fit to the molecule histogram below (red region) and above (green region) the intensity threshold (blue line).
6. A. The false negative probability, β , for the 155 pM concentration is plotted against the detection intensity threshold, n_{thold} . B. The false positive rate per 300 x 300 image for detection with three-pixel spatial correlation is plotted (log scale) against the detection intensity threshold, n_{thold} , for simulated results run on images of Poisson distributed random noise with $\mu = 13.0$ (black squares) and theoretical results from Equation 7 (black line). The false positive rate for detection using no pixel is also shown (black dashed line). The experimentally determined false positive rates with spatial correlation (red circle) and without spatial correlation (red triangle) are also plotted.

Table 1. Experimental Results for Quantitative Single Molecule Detection

R6G Solution Concentration	Experimental Spot Density, ¹ D_{meas} (1/cm ²)	Spot density uncertainty ² (1/cm ²)	Theoretical Spot Density, ³ D_{meas} (1/cm ²)	Mean Background, ⁴ μ_{BG} (photoelectrons)	Background Std. Dev., ⁵ σ_{BG} (photoelectrons)	Intensity Threshold, I_{thold} (photoelectrons)	False Negative Detection Probability, β (%)	Theoretical False Positive Probability, α_{theor} (per image)	Measured false Positive Probability, α_{exp} (per image)
Blank	3.6×10^5	6×10^4	0.0	13.0	3.6	22	-	1.9	2.8
20 pM	4.1×10^6	3×10^5	5.9×10^6	12.1	3.5	22	4.4 ⁶	1.9	-
40 pM	7.7×10^6	4×10^5	1.2×10^7	12.4	3.5	22	4.4 ⁶	1.9	-
79 pM	2.1×10^7	1×10^6	2.2×10^7	12.7	3.6	22	4.4 ⁶	1.9	-
155 pM	4.5×10^7	2×10^6	4.2×10^7	13.9	3.7	23	1.3	1.9	-
283 pM	7.6×10^7	4×10^6	7.1×10^7	17.0	4.1	27	1.7	1.9	-

¹ Blank densities have been subtracted from total densities for 20 to 283 pM R6G

² Uncertainty is 2 standard deviations of the mean

³ D_{meas} predicted by Equation 4.

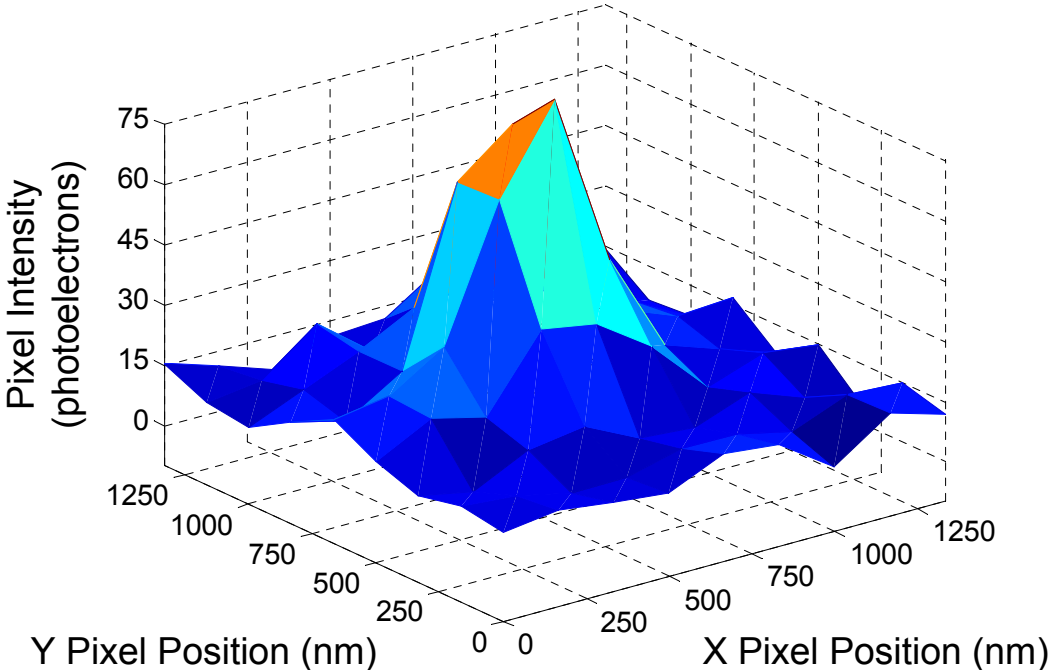
⁴ Determined by a Poisson distribution fit for the blank data, a Gaussian distribution for R6G samples (see text).

⁵ Calculated from mean: $\sigma_{\text{BG}} = \mu_{\text{BG}}^{1/2}$

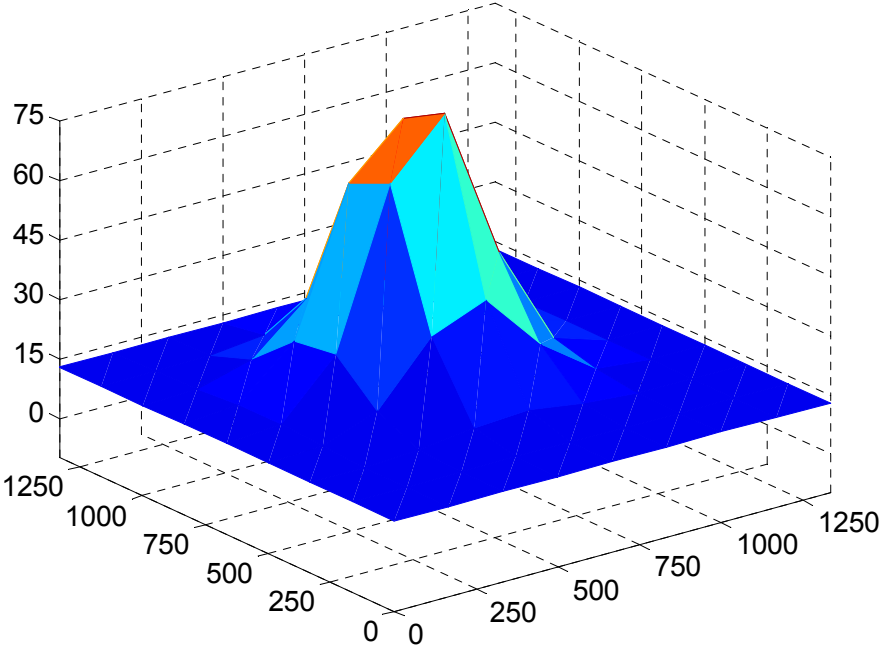
⁶ Histograms were summed for 20, 40, and 79 pM data

Figure 1

A



B



C

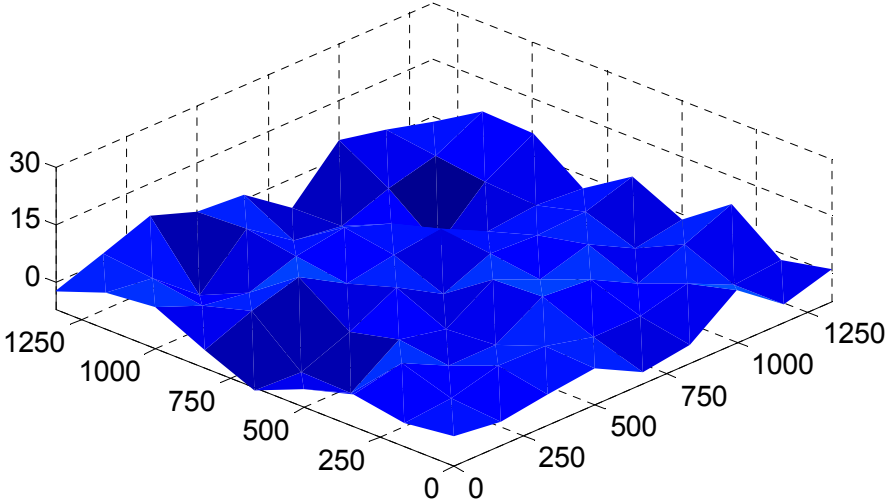


Figure 2

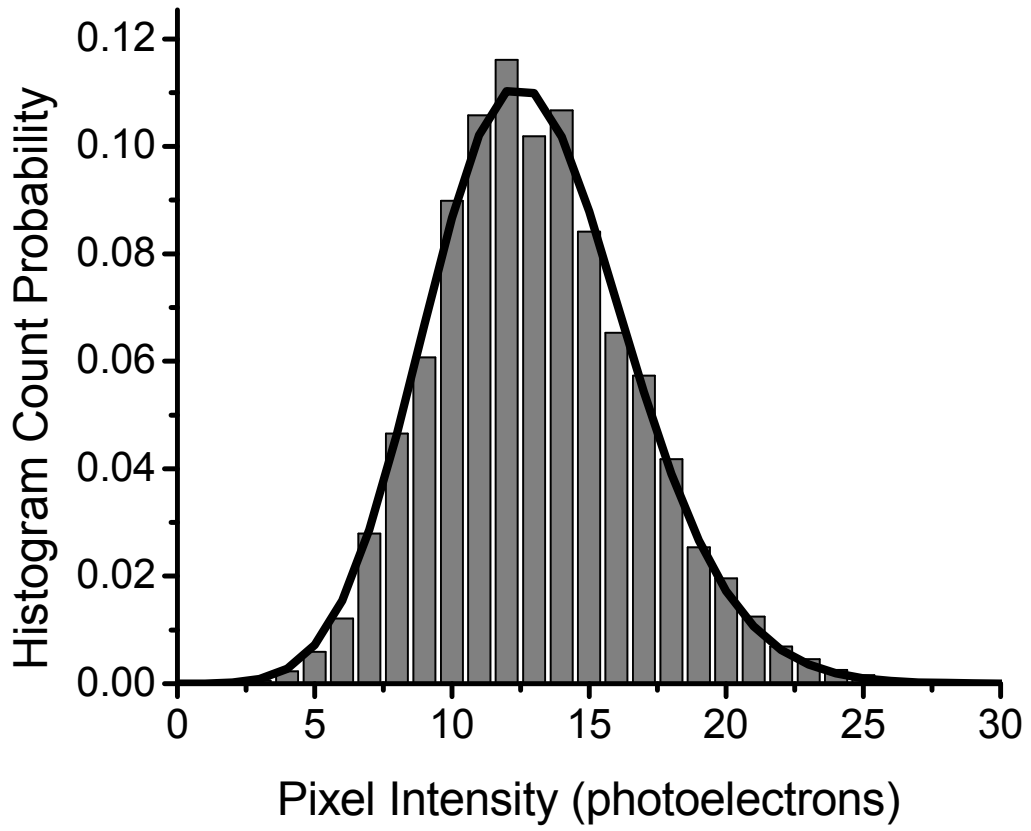


Figure 3

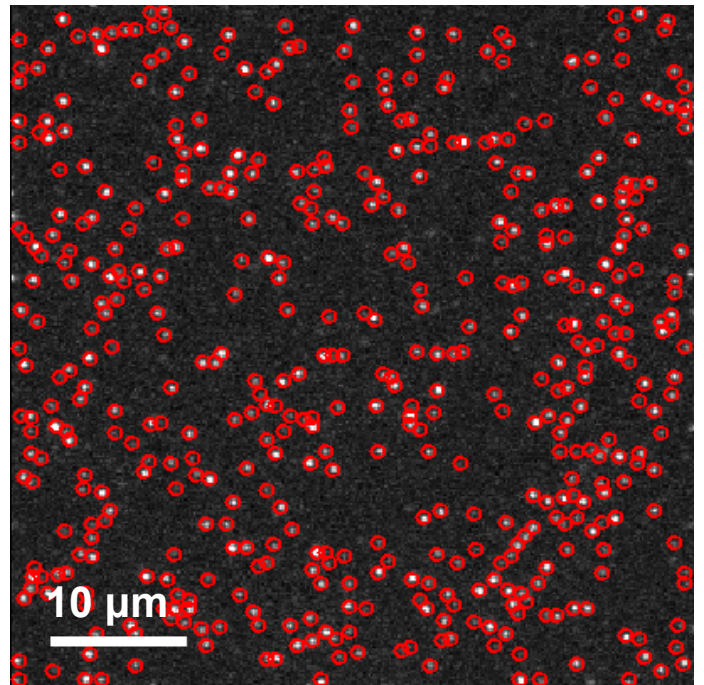
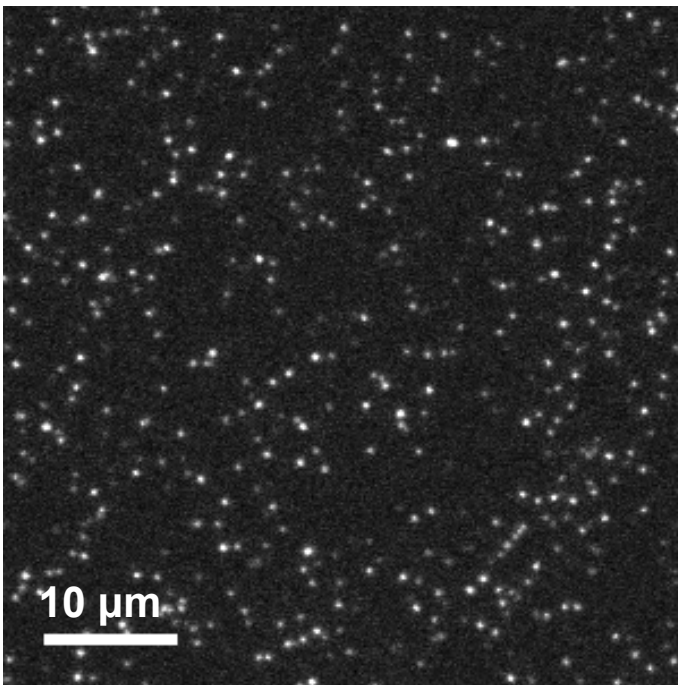


Figure 4

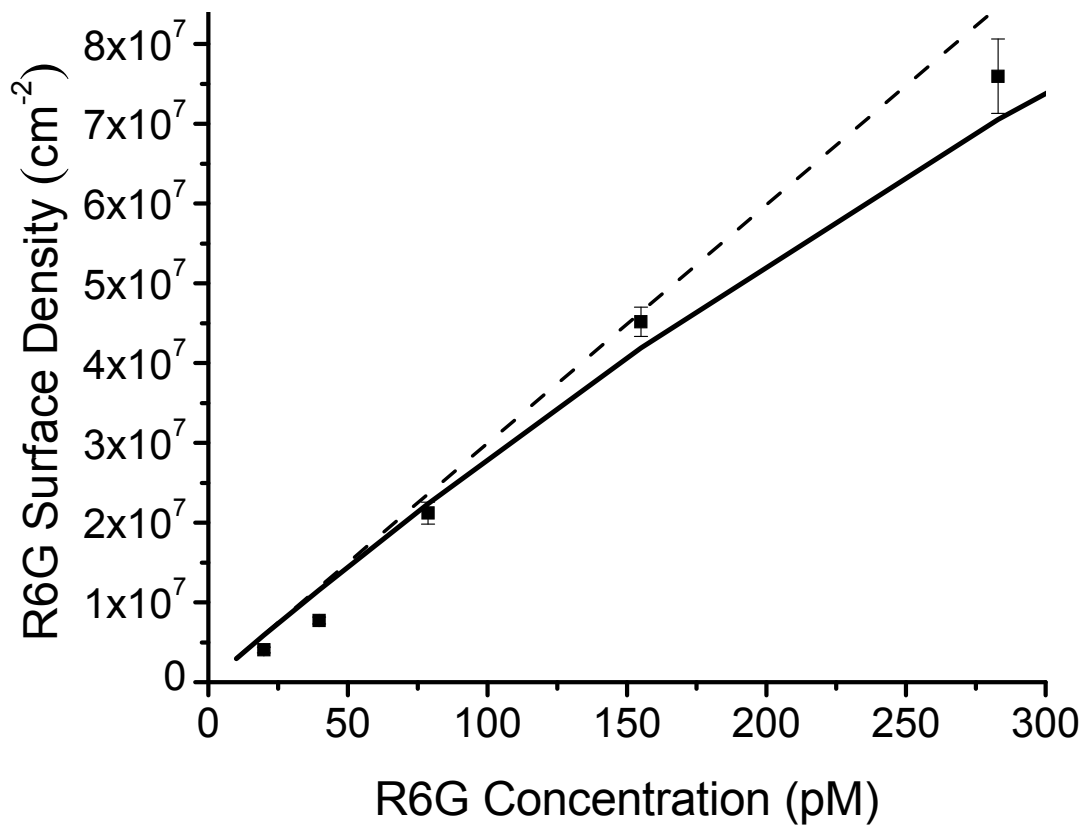


Figure 5

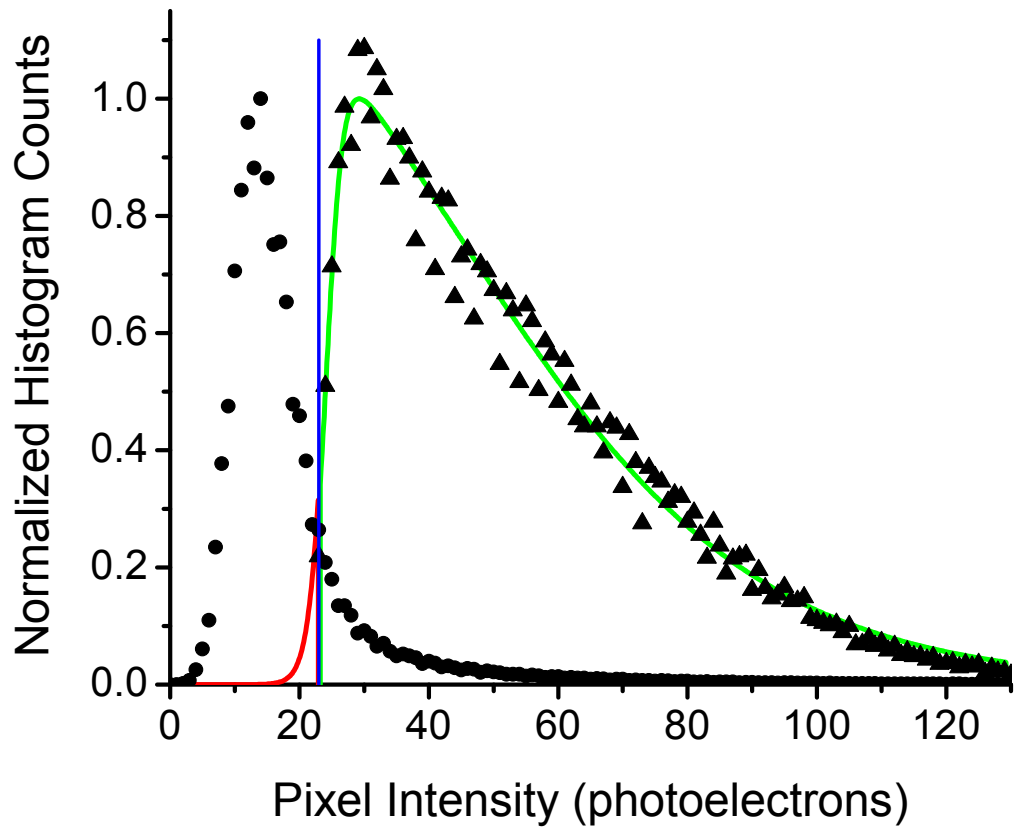


Figure 6

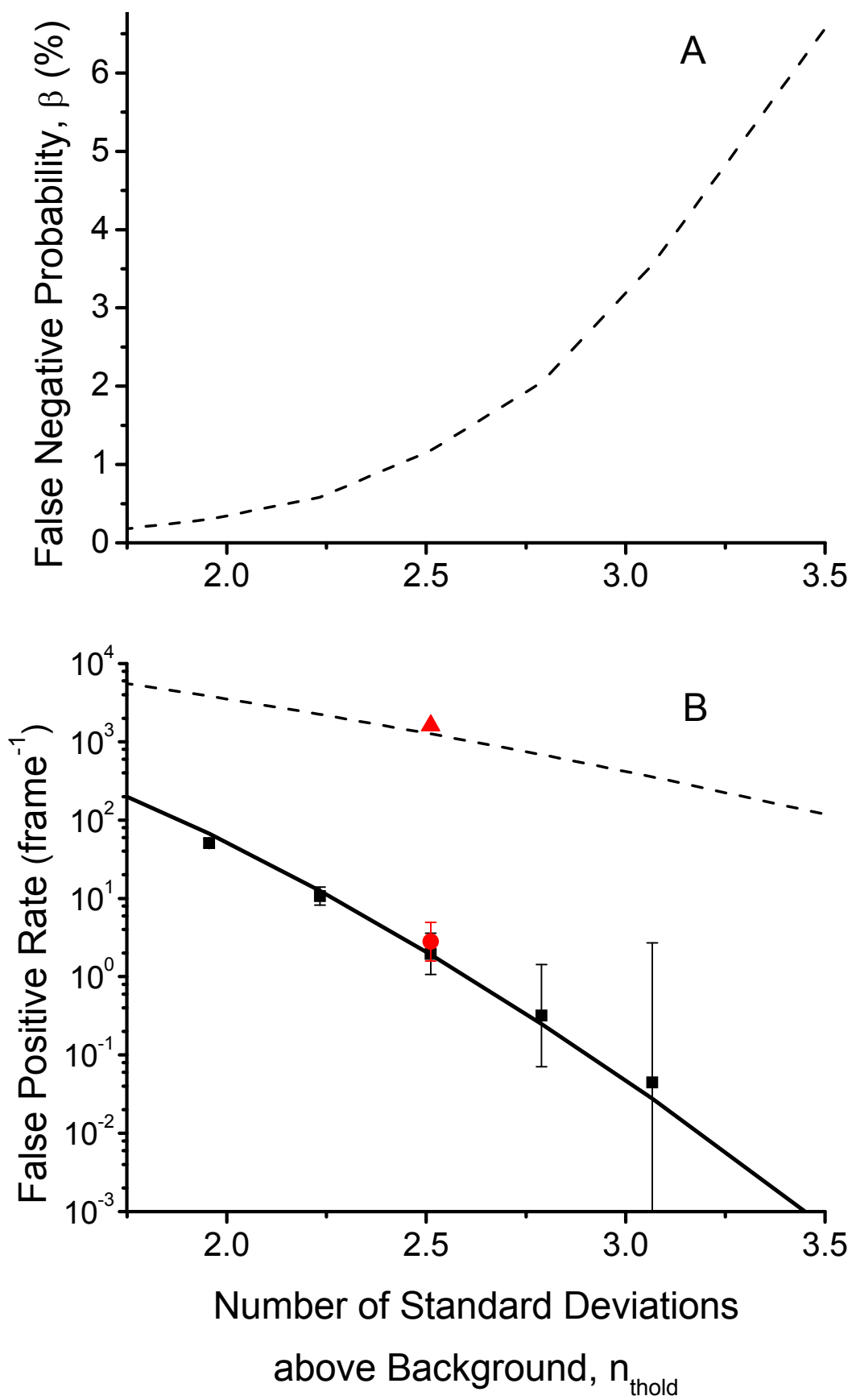
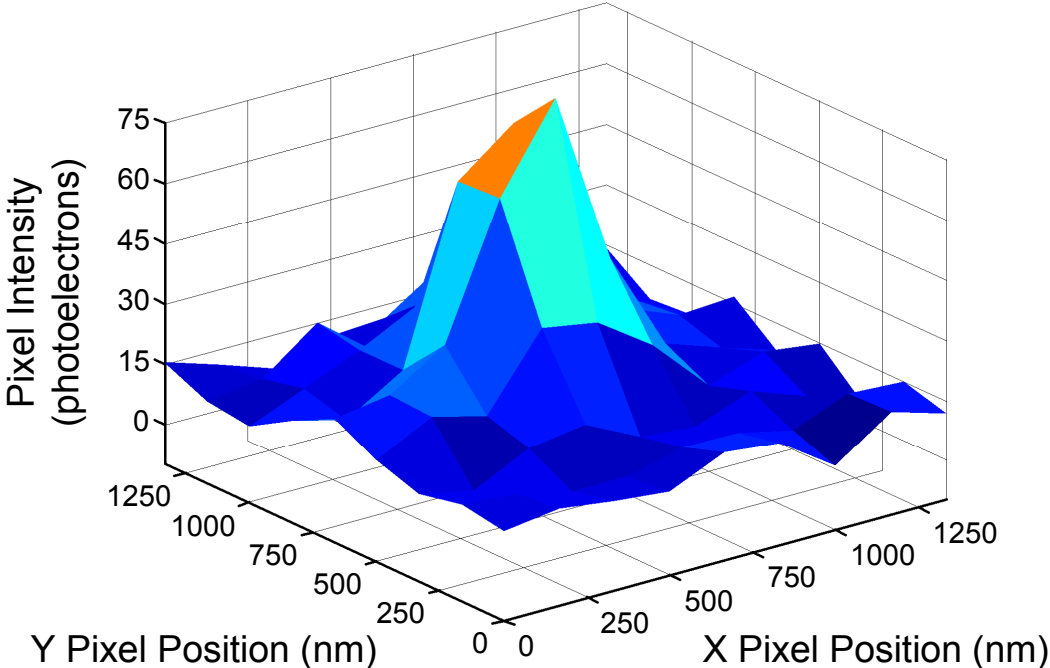
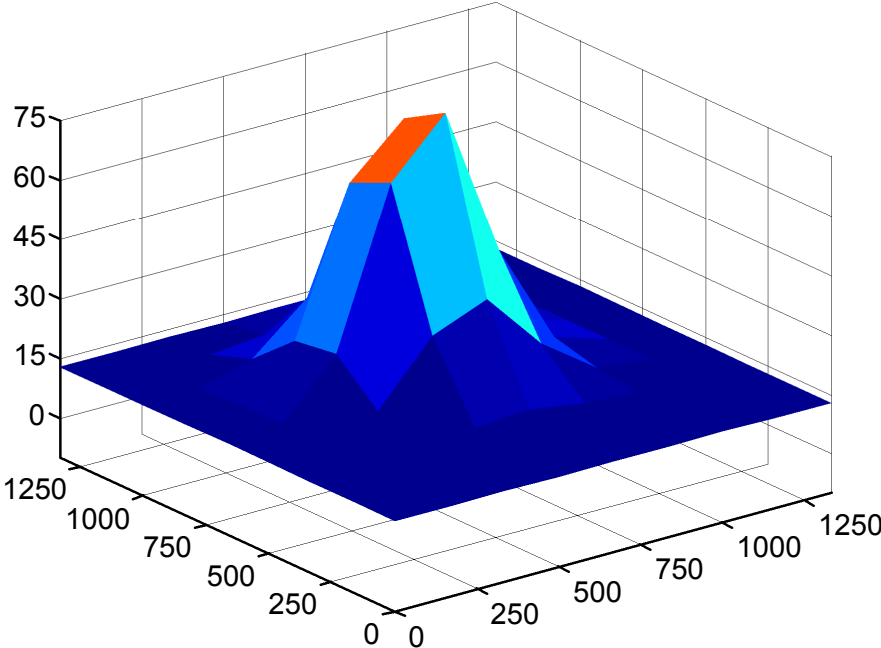


Figure 1

A



B



C

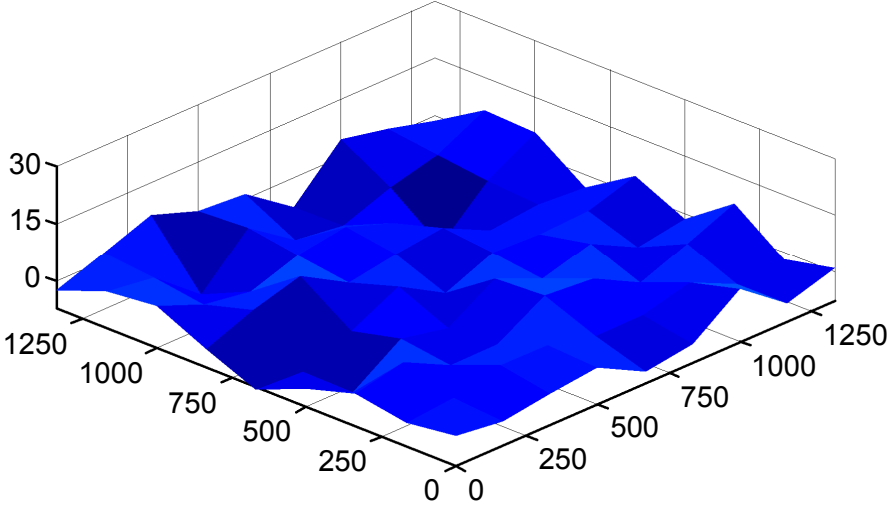


Figure 2

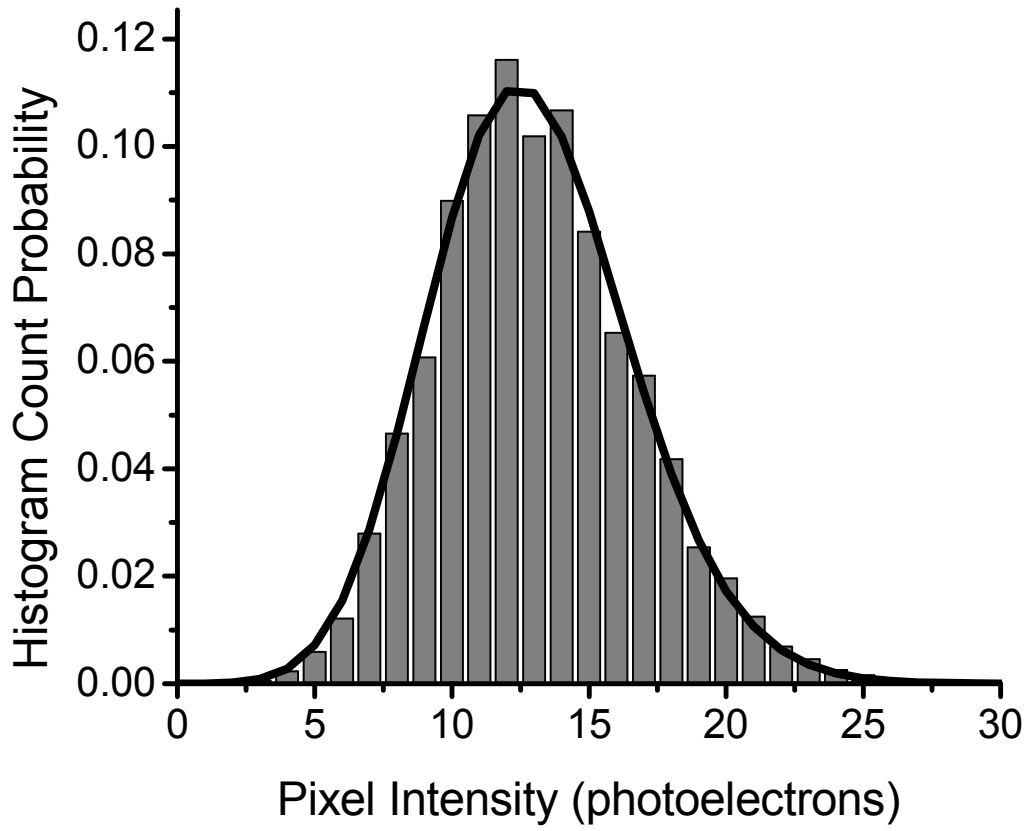


Figure 3

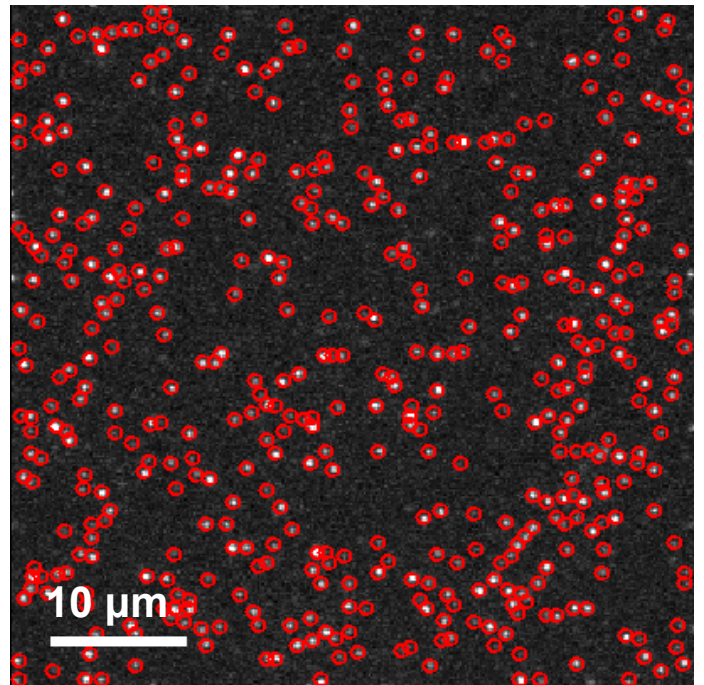
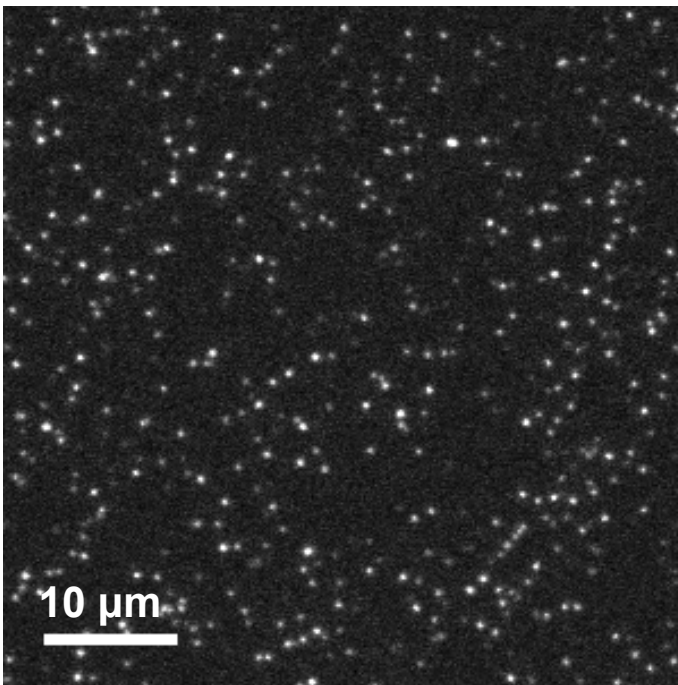


Figure 4

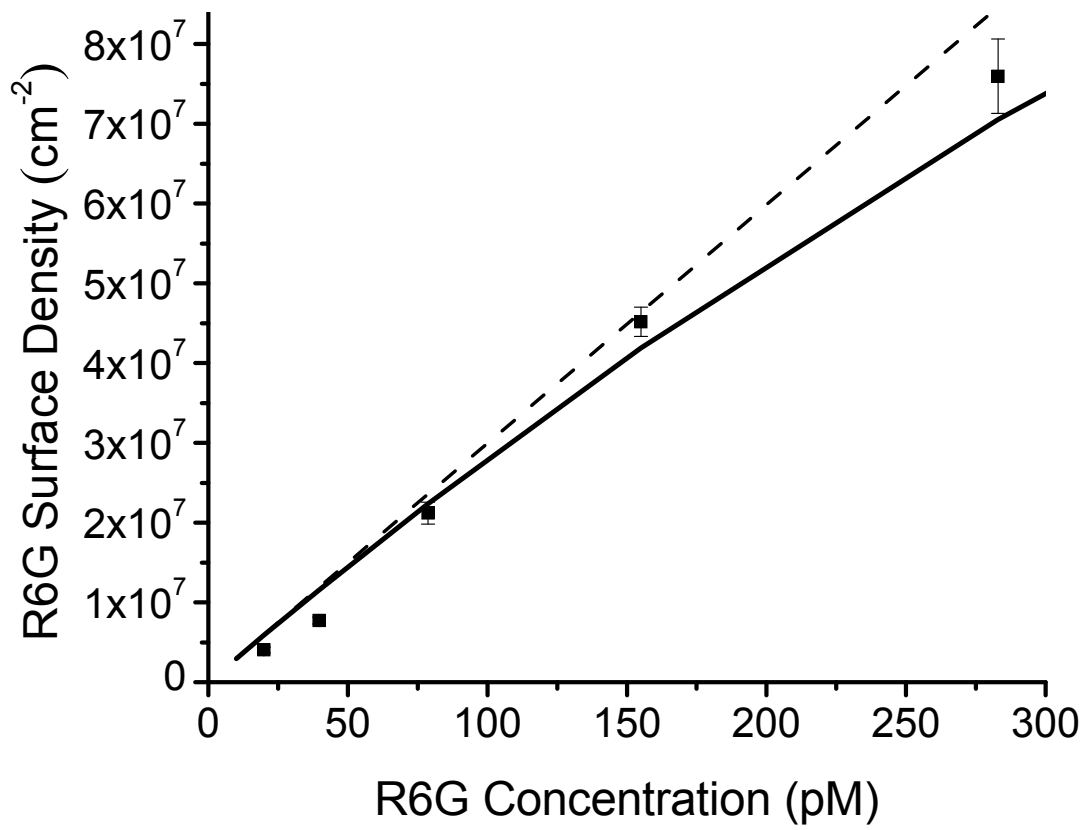


Figure 5

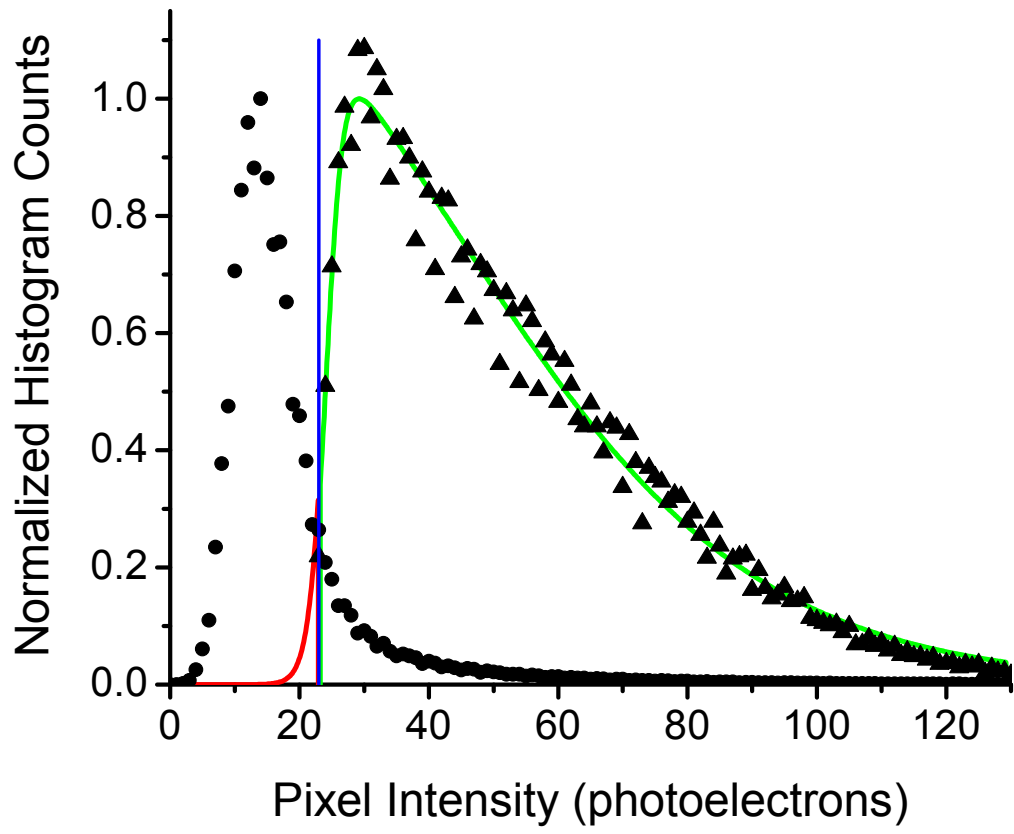


Figure 6

